ADVANCED FUNCTIONAL MATERIALS
www.afm-journal.de

Molybdate-Leaching-Induced Bimetallic Catalyst for Efficient Anion Exchange Membrane Water Electrolysis

*Zhuorong Lu, Wenzhe Niu, Yixiang He, Lujie Jin, Weihang Li, Xiao Yang, Kai Sun, Qisheng Yan, Jinyan Chen, Jiaqi Zhang, Wenjuan Shi, Chenyang Wei, Youyong Li, Hongbin Lu, and Bo Zhang**

Anion exchange membrane water electrolysis (AEMWE) offers a promising route for green hydrogen production avoiding noble metal catalysts. The sluggish oxygen evolution reaction (OER) kinetics constrained by the intrinsic activity and limited abundance of active sites however remains a significant barrier to the advancement of AEMWE. In this study, heteroatom doping is combined with a molybdate-leaching strategy to enhance both the intrinsic activity and active site abundance in a single catalyst. Iron is doped into nickel molybdate through a microwave-assisted method, followed by molybdenum leaching, formed molybdate-derived Fe-doped nickel hydroxide (MD-FeNi). The synergistic effects of the bimetallic composition and the expanded active surface area facilitate the transformation of $Ni(OH)_2$ in MD-FeNi to NiOOH, significantly enhancing OER activity. When integrated into an AEMWE system, the catalyst achieves an impressive current density of 7.48 A cm^{-2} at 2 V, which is ≈2.2 and 2.0 times higher than that of molybdate derived $Ni(OH)_2$ (3.35 A cm^{-2}) and traditional Fe doped $Ni(OH)_2$ (3.75 A cm^{-2}). Furthermore, this binary high-activity system strategy has demonstrated broad applicability across various catalytic systems, molybdate-derived Ag-doped copper hydroxide for high-efficient CO electroreduction and molybdate-derived Fe-doped cobalt hydroxide for $NaBH_4$ hydrolysis reaction, indicating its potential for diverse applications.

1. Introduction

Hydrogen production via water electrolysis powered by renewable electricity has emerged as a promising pathway for sustainable development.[1] However, traditional alkaline water electrolysis faces challenges due to high initial setup costs and limited current densities, making it less suitable for integration with renewable energy sources. Proton exchange membrane water electrolysis is considered a more viable option for "green hydrogen" production, offering rapid system response and high current densities. However, its dependence on noble metals (e.g., Ir, Ru) limits widespread adoption. Anion exchange membrane water electrolysis (AEMWE) presents an attractive alternative, combining rapid system response and high current density without requiring noble metals, making it a promising technology for sustainable hydrogen production.[2,3] Despite this potential, the practical application of AEMWE remains hindered by the slow reaction kinetics of the anodic oxygen evolution reaction (OER),[4–6] underscoring the need for easily synthesized, high-performance anodic catalysts.

Enhancing the number of active sites and improving their intrinsic activities are widely regarded as effective strategies for developing high-performance OER catalysts.[7,8] Atomic doping and alloying provide straightforward approaches to enhance the intrinsic activities of active sites through synergistic interactions between heteroatoms.[9–13] However, introducing non-active sites or phases can reduce the abundance of active sites, significantly limiting further improvements in catalytic performance.[1,14–16]

The instability of high-valence group VIB elements ($M^{\delta+}$, M = Cr, Mo, W; $\delta > 5$) in strong alkaline environments facilitates element leaching and redistribution, leading to the formation of open structures, such as fissures and pores, which expose additional active sites.[17–19] Previous studies have demonstrated that in certain molybdates, the leaching of Mo in alkaline solutions can induce a structural transformation into thin-layered, flake-like hydroxides, offering a simple method for synthesizing catalysts with a large active surface area.[20,21] However, most research

Z. Lu, W. Niu, Y. He, W. Li, X. Yang, K. Sun, Q. Yan, J. Chen, J. Zhang, C. Wei, H. Lu, B. Zhang
State Key Laboratory of Molecular Engineering of Polymers
Department of Macromolecular Science
Fudan University
Shanghai 200438, China
E-mail: bozhang@fudan.edu.cn
L. Jin, Y. Li
Institute of Functional Nano and Soft Materials (FUNSOM)
Jiangsu Key Laboratory for Carbon-Based Functional Materials & Devices
Soochow University
Suzhou, Jiangsu 215123, China
W. Shi
School of Marine Science and Engineering
State Key Laboratory of Marine Resource Utilization in South China Sea
Hainan University
Haikou 570228, China

The ORCID identification number(s) for the author(s) of this article can be found under https://doi.org/10.1002/adfm.202505626

DOI: 10.1002/adfm.202505626

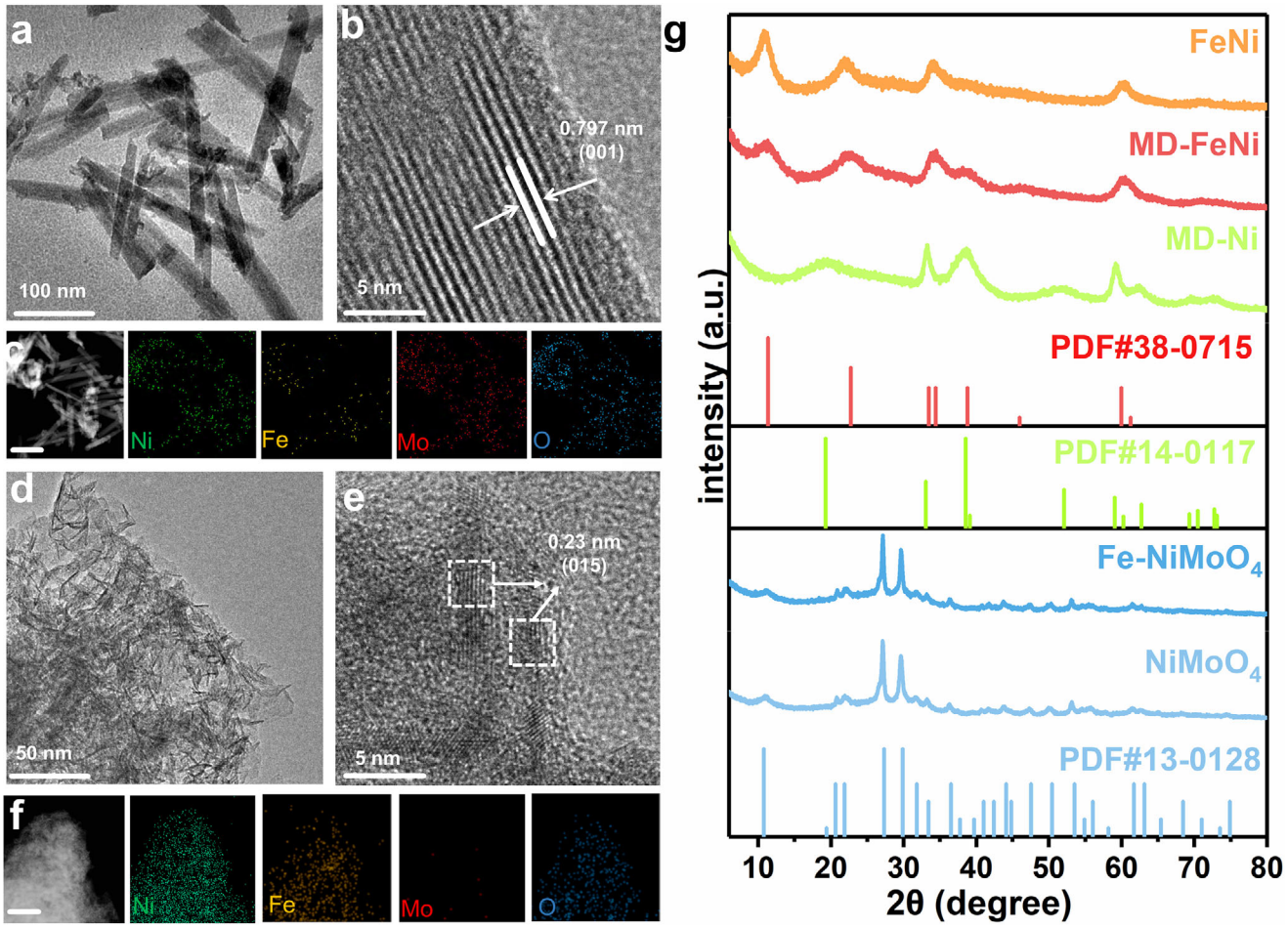

Figure 1. Catalysts synthesis and characterization. a,b,d,e) HRTEM images of Fe-$NiMoO_4 \cdot xH_2O$ a, b) and MD-FeNi d, e) and the corresponding lattice spacing. c,f) EDS mapping of Fe-$NiMoO_4 \cdot H_2O$ c) and MD-FeNi f). g) XRD patterns of $NiMoO_4 \cdot xH_2O$, Fe-$NiMoO_4 \cdot xH_2O$, MD-Ni, MD-FeNi and FeNi. The scale bar in Figure 1c,d is 100 nm.

has focused on monometallic catalysts, limiting their broader applicability.[22,23] We hypothesized that incorporating a second metal into catalysts with a high active surface area could further enhance catalytic activity.[24,25]

In this work, we combined heteroatomic doping with a molybdate-leaching-induced structural reconstruction strategy to develop high-performance catalysts with both high intrinsic activity and abundant active sites. We report a facile synthesis of MD-FeNi, reconstructed through Mo leaching from a $NiMoO_4 \cdot xH_2O$ precursor. The Fe dopants modulate the electronic structure of Ni active species by facilitating partial charge transfer between heteroatoms, significantly enhancing the OER performance of the molybdate-derived Fe-doped nickel hydroxide (MD-FeNi) compared to the molybdate-derived nickel hydroxide (MD-Ni).[26–31] Moreover, the Mo leaching-induced re-construction remarkably increased the electrochemical surface area (ECSA) of the MD-FeNi, exposing more active sites and further boosting its OER performance. Operando spectroscopic analysis revealed that the highly exposed active surface area and bimetallic system promote the formation of metal oxyhydroxides as active OER species, contributing to superior catalytic activity. Consequently, when integrated into an AEMWE system, the catalyst achieved an ultra-low voltage of 1.61 V at a current density of 1.00 A cm^{-2} and demonstrated stable operation for over 280 h. Notably, the catalyst delivers a high current density of 7.48 A cm^{-2} at 2.0 V, highlighting its exceptional catalytic reactivity. Furthermore, this strategy for constructing highly active bimetallic systems has proven versatile and can be extended to catalysts for CO electrochemical reduction reactions (CORR) and sodium borohydride hydrolysis (SBH).

2. Results and Discussion

2.1. Catalysts Synthesis and Characterization

$NiMoO_4 \cdot xH_2O$ and Fe-$NiMoO_4 \cdot xH_2O$ were synthesized by microwave method. X-ray diffraction (XRD) patterns of $NiMoO_4 \cdot xH_2O$ and Fe-$NiMoO_4 \cdot xH_2O$ powders (**Figure 1g**) exhibit three main characteristic peaks of $NiMoO_4 \cdot xH_2O$ at 2θ values of 10.98°, 27.14°, and 29.64° (JCPDS No. 13–0128). Transmission electron microscopy (TEM) images show that $NiMoO_4 \cdot xH_2O$ and Fe-$NiMoO_4 \cdot xH_2O$ both exhibit rod-like morphology ranging in size from 40 to 100 nm (Figure 1a; Figure S1a, Supporting Information). Lattice spacings of 0.797 and 0.209 nm shown in the high-resolution TEM (HRTEM) images

can be attributed to the (001) and (111) plane of $NiMoO_4 \cdot xH_2O$, respectively[32,33] (Figure 1b; Figure S1b, Supporting Information). Selected area electron diffraction (SAED) of Fe-$NiMoO_4 \cdot xH_2O$ also reveals the presence of the (001) and (002) crystal planes of $NiMoO_4 \cdot xH_2O$, consistent with the results obtained from HRTEM (Figure S2a, Supporting Information). Energy dispersive X-ray spectroscopy (EDS) elemental mapping indicates that Fe was uniformly doped into the $NiMoO_4 \cdot xH_2O$ crystal without disrupting the crystal lattice (Figure 1c; Figure S3, Supporting Information). Both the XRD patterns and TEM images demonstrate the successful synthesis of the two samples.

Afterward, $NiMoO_4 \cdot xH_2O$ and Fe-$NiMoO_4 \cdot xH_2O$ powders were treated in an alkaline solution to remove molybdate ions, resulting in the formation of thin-film hydroxide catalysts (denoted as MD-Ni and MD-FeNi, respectively). In addition, traditional Fe-doped nickel hydroxide (FeNi) was synthesized through a precipitation microwave method. The reconstruction of $NiMoO_4 \cdot xH_2O$ and Fe-$NiMoO_4 \cdot xH_2O$ to MD-Ni and MD-FeNi, as well as the synthesis of FeNi, are demonstrated by XRD and TEM. In Figure 1g, the XRD patterns of MD-Ni show three main characteristic peaks at 18.7°, 33.22°, and 38.18°, corresponding to β-$Ni(OH)_2$ (JCPDS No. 14–0117). The XRD patterns of MD-FeNi and FeNi reveal four characteristic peaks of α-$Ni(OH)_2$ at 11.14°, 22°, 34°, and 38.3° (JCPDS No. 38–0715), confirming their main crystalline structure. TEM images illustrate that the MD-Ni and MD-FeNi are highly dispersed thin-layered flaky nanocrystals, while FeNi shows a high-density agglomeration of crystals (Figure 1d; Figures S2b,S4a, and S5a, Supporting Information). The lattice spacing of 0.179 nm observed in the TEM image corresponds to the (102) plane of β-$Ni(OH)_2$ (Figure S4b, Supporting Information). The TEM images reveal lattice spacings of 0.230 and 0.236 nm, corresponding to the (015) plane of α-$Ni(OH)_2$ (Figure 1e; Figure S5b, Supporting Information). EDS elemental mapping shows that Mo species in $NiMoO_4 \cdot xH_2O$ and Fe-$NiMoO_4 \cdot xH_2O$ were completely dissolved after alkali treatment (Figure 1f; Figures S3b and S4c, Supporting Information), which was also proved by inductively coupled plasma optical emission spectrometer (ICP-OES). Moreover, the results of ICP-OES also indicate that Fe-$NiMoO_4 \cdot xH_2O$ contains Fe, Ni, and Mo, with a molar ratio of ≈1.0:4.5:5.5, whereas in MD-FeNi, the molar ratio approaches 1.0:4.0:0, resembling that of FeNi (Table S1, Supporting Information). The catalyst synthesized under these conditions exhibited optimal OER performance (Figures S6 and S7 and Table S2, Supporting Information).

In addition, in situ Raman spectra of $NiMoO_4 \cdot xH_2O$ and Fe-$NiMoO_4 \cdot xH_2O$ of different immersion times in 1 M KOH were collected in Figure S8 (Supporting Information). Prior to soaking, the Raman spectra of $NiMoO_4 \cdot xH_2O$ and Fe-$NiMoO_4 \cdot xH_2O$ exhibit similar peaks. The peak at 348 cm^{-1} corresponds to the asymmetric bending mode of O—Mo—O connections. After soaking in an alkaline solution, the peak intensity of 348 cm^{-1} in $NiMoO_4 \cdot xH_2O$ gradually decreases, while two broad peaks at 318 and 453 cm^{-1} emerge with increasing intensity, which is attributed to the E_g and A_{1g} modes of β-$Ni(OH)_2$.[21,34,35] In contrast, the characteristic peak of molybdate in Fe-$NiMoO_4 \cdot xH_2O$ immediately disappears, and three broad peaks appear at 305, 456, and 523 cm^{-1}, corresponding to the E_g mode in β-$Ni(OH)_2$ as well as the E_g and A_{1g} modes in α-$Ni(OH)_2$.[36,37] No peaks related to Fe-O are observed,[38,39] indicating that Fe does not form a separate phase, which is consistent with the XRD results (Figure 1g). In situ, Raman spectra illustrated the gradual loss of Mo species during soaking in alkaline solution and revealed that the surface of MD-FeNi contained a small amount of β-$Ni(OH)_2$.

2.2. Electrocatalytic Performance

The catalytic performance of different catalysts was evaluated in 1 M KOH solution at 25 °C. Linear sweep voltammetry (LSV) curves demonstrate that MD-FeNi shows a higher OER activity with the lowest overpotential (256 mV) at 100 mA cm^{-2}, compared to MD-Ni (298 mV) and FeNi (324 mV) (**Figure 2a**; Figure S9, Supporting Information). This performance is also considered to be advanced in recent studies (Table S3, Supporting Information). Subsequently, the reaction kinetics of the catalysts were evaluated by Tafel plots and electrochemical impedance spectroscopy (EIS). As shown in Figure S10a (Supporting Information), the Tafel slope of MD-FeNi is merely 39 mV dec^{-1}, which is considerably lower than that of MD-Ni (121 mV dec^{-1}) and FeNi (79 mV dec^{-1}), indicating its superior reaction kinetic. The charge transfer resistance (R_{ct}) of MD-FeNi (20.8 Ω) is much lower than that of MD-Ni (138 Ω) and FeNi (898 Ω) catalysts obtained by EIS curve fitting at 1.4 V (Figure S10b, Supporting Information). Additionally, our density of state (DOS) calculations show that Fe doping shifts the Ni d-band center and narrows the bandgap of the material, making it easier to gain or lose electrons. As a result, R_{ct} decreases during the reaction process, which is consistent with the EIS results (Figure S11, Supporting Information).

We hypothesized that the leaching of molybdenum species could effectively increase the ECSA, thus enhancing the OER activity. This was verified by measuring the ECSAs of different catalysts (Figure 2b; Figure S12, Supporting Information). Both MD-FeNi and MD-Ni show similar electrochemical active areas (10.6 and 10.8 cm^{-2}), substantially larger than that of traditional FeNi (1.5 cm^{-2}). Therefore, the depletion of Mo species could significantly increase the ECSA of the catalyst, fully proving the increase of active sites. Additionally, MD-FeNi and MD-Ni may exhibit either one or two broad peaks within the range of 1.35-1.50 V, likely due to the increased active sites reducing local charge accumulation, resulting in a smoother and more continuous oxidation process[19] (Figure S13, Supporting Information). ECSA-normalized LSV further demonstrated that the intrinsic activities of MD-FeNi and FeNi catalysts were similar, and the activity enhancement of MD-FeNi was mainly caused by the increased electrochemically active surface area.

We further investigated the practical application of MD-FeNi and other catalysts as an anodic catalyst AEMWE system (Figure 2d,e; Figure S14, Supporting Information). MD-FeNi could achieve a high current density of 7.48 A cm^{-2} at 2.0 V, which is ≈2.2 and 2.0 times higher than that of MD-Ni (3.35 A cm^{-2}) and FeNi (3.75 A cm^{-2}), respectively (Figure 2d; Figure S15, Supporting Information). And MD-FeNi operated stably in AEMWE for 50 min at 25 °C and 7.48 A cm^{-2}, with an average Faradaic efficiency (FE) of 97.1%, and demonstrating considerable microstructural stability (Figures S16–S18, Supporting Information). Furthermore, the long-term stability of the electrolyzer was evaluated in 1 M KOH at 1.00 A cm^{-2}. As shown in Figure 2e, MD-FeNi exhibits remarkable stability, maintaining a low voltage range of 1.61–1.64 V for over 280 h, with a degradation rate

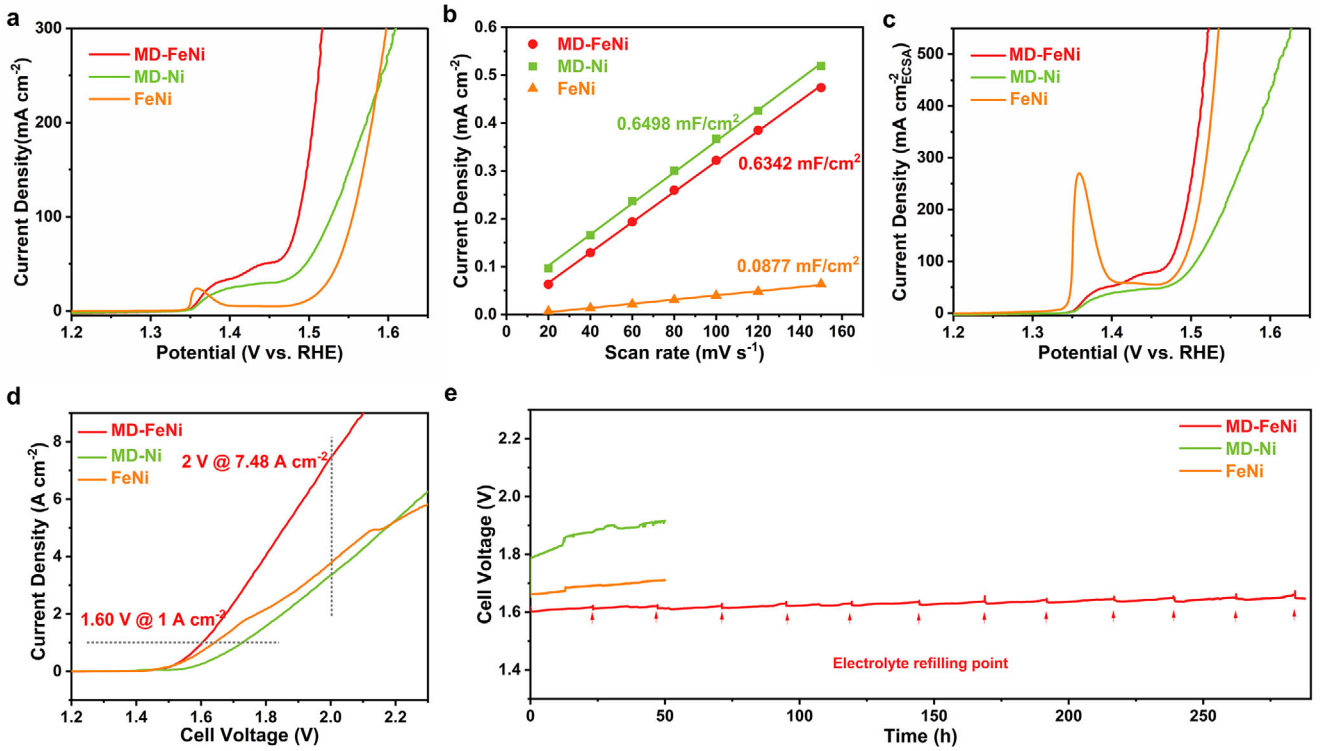

Figure 2. Electrocatalytic performance. a) Linear sweep voltammetry curves in a three-electrode system recorded for MD-Ni, MD-FeNi, and FeNi, with 80% manual iR correction. The measurements were conducted with a scan rate of 5 mV s^{-1}. b) ECSA measurement and c) LSV curves normalized by ECSA of MD-Ni, MD-FeNi, and FeNi in a three-electrode system. d) Linear sweep voltammetry curves of the 1 cm^2 electrolyzer applied with MD-Ni, MD-FeNi, and FeNi at 80 °C in 1 M KOH. e) Stability of the 5 cm^2 electrolyzer applied with MD-Ni, MD-FeNi, and FeNi measured at 1.00 A cm^{-2} and 60 °C. The strong peaks at 1.36 V versus RHE in the LSV curve correspond to the oxidation of Ni.

of 0.1 mV h^{-1}, significantly outperforming MD-Ni and FeNi. This performance positions it among the most advanced reported AEM electrolysis performances to date (Table S4, Supporting Information), and further demonstrates that molybdate leaching reconstruction and bimetallic synergistic effect can enhance the performance of the catalyst. Additionally, comparative analysis of X-ray Photoelectron Spectroscopy (XPS), XRD, TEM, and Scanning Electron Microscope (SEM) for MD-FeNi before and after AEMWE operation revealed negligible alterations in its oxidation states, crystalline structure, and morphology, confirming its robust stability under operational conditions (Figure 1d,e; Figures S19–S24, Supporting Information).

2.3. In Situ Structural Research

Potential-dependent in situ Raman spectroscopy was utilized to characterize the formation of a real active site (NiOOH) during the OER process. As shown in **Figure 3**b, at low applied potential (1.3 V vs RHE), MD-Ni exhibits two broad Raman peaks at 318 and 453 cm^{-1}, corresponding to the E_g and A_{1g} lattice modes of β-$Ni(OH)_2$. In contrast, MD-FeNi and FeNi display three broad peaks at 305, 456, and 523 cm^{-1}, corresponding to the E_g mode of β-$Ni(OH)_2$ and the E_g and A_{1g} modes of α-$Ni(OH)_2$, respectively (Figure 3a,c). As the applied potential increased to 1.4 V, two new peaks appeared for MD-FeNi at 470 and 552 cm^{-1}, which are attributed to the E_g and A_{1g} modes of NiOOH,[21,34–37] while the Raman peaks associated with $Ni(OH)_2$ disappeared. In contrast, the Raman spectra of MD-Ni and FeNi indicate that $Ni(OH)_2$ began to be oxidized to NiOOH at a higher applied potential of 1.5 V, with the peak intensity of β-$Ni(OH)_2$ in MD-Ni decreasing gradually.

In line with the previous discussion, these results clarify the role of the Mo leaching strategy: it facilitates the formation of smaller crystal domains without altering the Ni oxidation state (Figure 1d; Figures S5b and S25, Supporting Information), and the increased disorder significantly enhances the ECSA of MD-FeNi compared to FeNi (Figure 2b), exposing a large number of active sites. This allows for faster generation of NiOOH active species, resulting in superior OER performance.

We further studied the mechanism of Fe doping. It is established that MD-Ni exhibits a morphology and structure similar to those of MD-FeNi (Figure S4b, Supporting Information), and O1*s* XPS does not show any evidence of oxygen vacancies (Figure S19c and S24b, Supporting Information). Therefore, we speculate that Fe doping modulates the electronic structure of $Ni(OH)_2$. The XPS Ni 2*p* spectra of MD-FeNi and MD-Ni reveal two primary spin–orbit peaks (Ni $2p^{1/2}$ and Ni $2p^{3/2}$) along with two corresponding shake-up satellite peaks. The presence of distinct peaks at 855.3 and 857.0 eV in the Ni $2p^{3/2}$ region indicates the existence of Ni^{2+} and Ni^{3+} (Figure S19a and S26a, Supporting Information).[40] While there is no significant shift in the peak positions between MD-FeNi and MD-Ni, a comparison of the Ni^{2+}/Ni^{3+} ratio for both samples in Figure S26b (Supporting

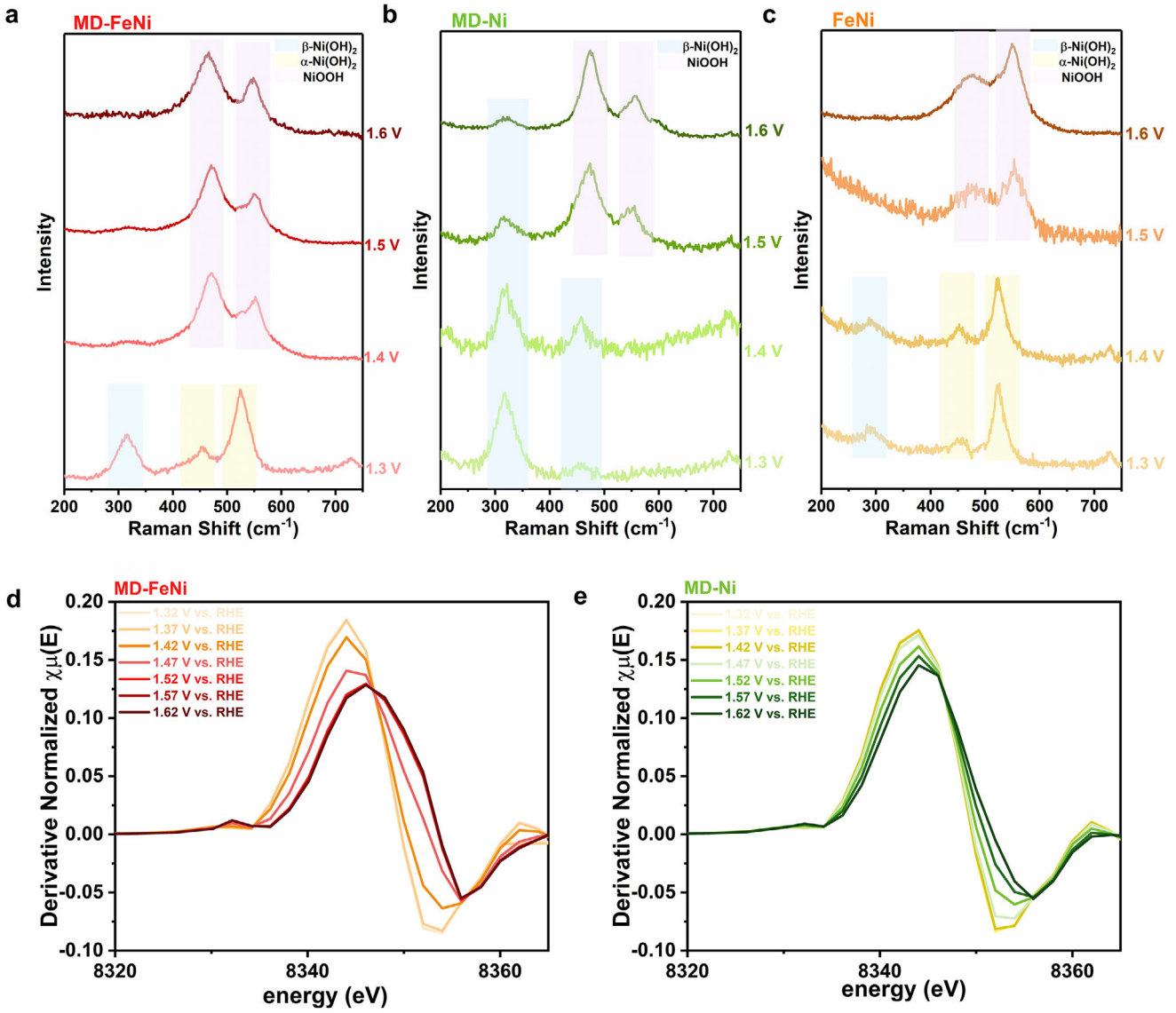

Figure 3. In situ mechanism research. a–c) Potential-dependent in situ Raman spectroscopy measurements of MD-FeNi a), MD-Ni b) and FeNi c) in 1 M KOH. d,e) The first derivative of in situ Ni K-edge X-ray Absorption Near Edge Structure (XANES) spectroscopy of MD-FeNi (d) and MD-Ni (e).

Information) reveals a significant increase in the oxidation state of Ni after Fe doping.

X-ray absorption spectroscopy then provided insights into the changes in the oxidation state and electronic structure of Ni during the reactions of MD-Ni and MD-FeNi. In situ, Ni K-edge X-ray absorption near edge structure (XANES) spectroscopy was applied to further confirm that MD-FeNi was more easily oxidized. The white line (expressed as the maximum value in the first derivative of Ni K-edge XANES, Figure 3d,e) of MD-FeNi shifts downward obviously at 1.42 V (vs RHE) and remains constant above 1.52 V. In contrast, the white line of MD-Ni begins to shift downward at 1.47 V and stabilizes at 1.62 V (Figure 3e). These results show that incorporating Fe into the pre-catalyst could also accelerate the formation of active species, thereby enhancing catalytic activity. Extended X-ray absorption fine structure (EXAFS) spectra and fitting analysis (Figures S27 and S28 and Table S5, Supporting Information) revealed a reduction in the coordination number of Ni-O and Ni—Ni, and a decrease in bond lengths of Ni—O and Ni—Ni paths.[41] This structural distortion likely exposes undercoordinated Ni sites, which act as precursors for NiOOH formation,[34,42] consistent with the in situ Raman results.

Finally, we conducted a further supplementary analysis using DFT calculations. Bader charge analysis (Figure S29, Tables S6 and S7, Supporting Information) further confirms an increase in the oxidation state of Ni, consistent with our XPS and XANES results, suggesting that Fe incorporation facilitates charge redistribution within the catalyst.

Furthermore, we have calculated the Gibbs free energy (ΔG) change for the *OOH formation step (Figure S30, Supporting Information), which is identified as the rate-determining step (RDS).[43,44] Our results indicate that Fe doping lowers the

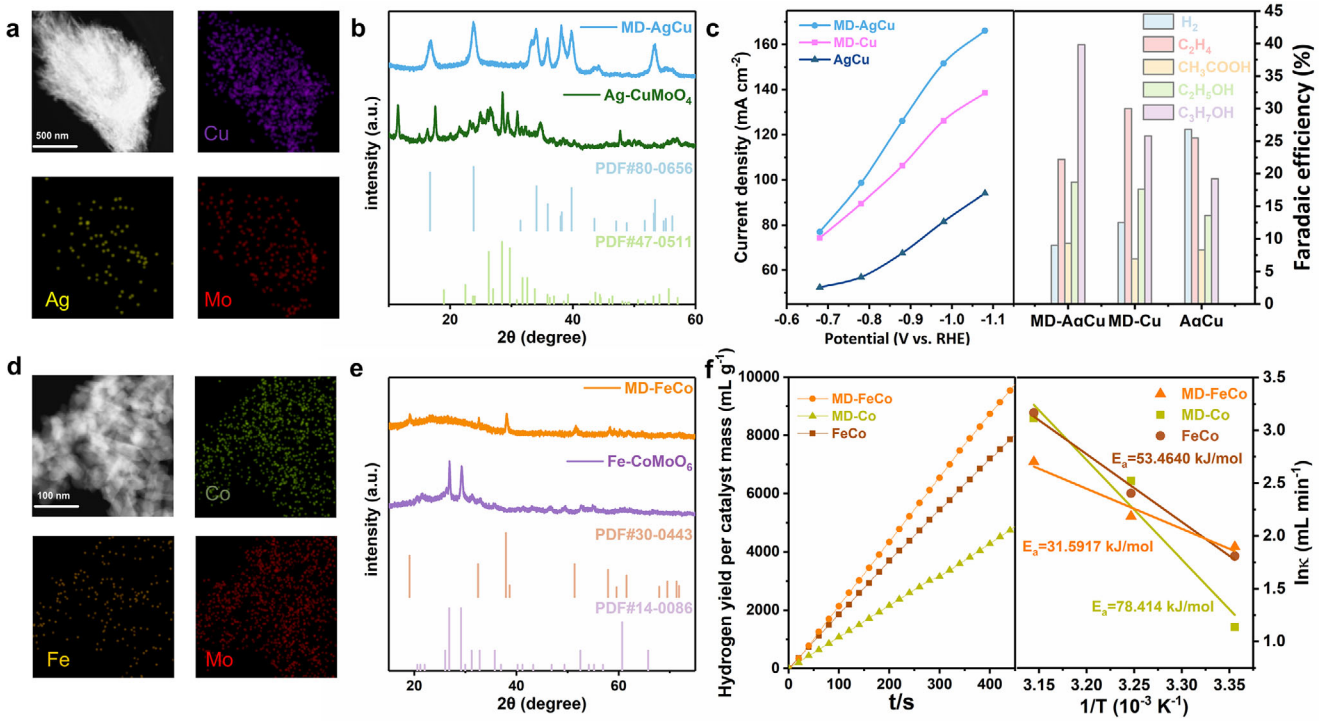

Figure 4. Characterization of materials to validate extensibility. a) EDS mapping of Ag-$CuMoO_4$. b) XRD patterns of Ag-$CuMoO_4$ and MD-AgCu catalysts. c) The current density of Ag-$CuMoO_4$ and MD-AgCu catalysts to produce propanol at a potential from −0.68 to −1.68 V versus RHE. and CORR products distribution under −0.98 V versus RHE on Ag-$CuMoO_4$ and MD-AgCu catalysts. d) EDS mapping of Ag-$CuMoO_4$. e) XRD patterns of Fe-$CoMoO_6$ and MD-FeCo. f) SBH performance of the MD-FeCo, MD-Co, and FeCo catalysts in 2 wt.% $NaBH_4$ at 25 °C and the corresponding Arrhenius plots of the MD-FeCo, MD-Co and FeCo catalysts.

energy barrier for this step, thereby improving OER catalytic performance.

The combined experimental and computational data demonstrate that Fe doping modulates the electronic structure of $Ni(OH)_2$, facilitating the oxidation of Ni species to higher valence states (Ni^{3+}) and lowering the ΔG of the RDS, thereby significantly enhancing the OER performance of the catalyst.

2.4. Application of Bimetallic Molybdate Pre-Catalysts in Other Systems

Finally, the extensibility of strategies involving molybdate-leaching-induced bimetallic catalysts was studied in the CORR and SBH systems. For CORR, Ag-$CuMoO_4$ was initially synthesized using the same method. XRD in **Figure** 4b revealed characteristic peaks of $CuMoO_4$ at 23.8° and 26.4°. TEM images and EDS mapping confirmed the uniform distribution of Ag (Figure 4a; Figure S31, Supporting Information). The molybdate-derived Ag-doped $Cu(OH)_2$ (MD-AgCu) was obtained by immersing the Ag-$CuMoO_4$ pre-catalyst in an alkaline solution. The obtained sample was also studied by XRD and TEM (Figure 4a; Figures S32 and S33, Supporting Information). The XRD peaks at 16.7° and 29.8°, could be attributed to $Cu(OH)_2$ (JCPDS no. 80–0656). For comparison, we also synthesized molybdate-derived $Cu(OH)_2$ (MD-Cu) and Ag-doped $Cu(OH)_2$ (AgCu) with similar atomic ratios (Table S8, Supporting Information).

Subsequently, the CORR performance of the three catalysts was evaluated using a potentiostatic flow cell reactor with 1 M KOH electrolyte. Among them, MD-AgCu exhibits the highest current density for the production of propanol (Figure 4c), indicating that its half-cell energy efficiency for CO electrochemical conversion to propanol significantly outperformed that of the other two catalysts. As shown in Figure 4c, MD-AgCu achieves the highest FE for C_{2+} products across various potentials. At -0.98 V, the FE for C_{2+} products from MD-AgCu reaches 90%, which is 1.12 and 1.35 times higher than MD-Cu and AgCu, respectively. Additionally, the FE of MD-AgCu for propanol also shows significant improvements, being 1.54 and 2.07 times higher than that observed on MD-Cu and AgCu, respectively.

As for the promoting mechanism, our results illustrate that doping Ag into Cu-based catalysts can significantly enhance the FE for propanol, consistent with previous reports.[45,46] Moreover, it is found that the ECSA of MD-AgCu is considerably larger than that of AgCu (Figure S34, Supporting Information), leading to further improvement in the FE for C_{2+} products.

For SBH systems, we synthesized the molybdate-derived Fe-doped $Co(OH)_2$ (MD-FeCo), the molybdate-derived $Co(OH)_2$ (MD-Co), and the Fe-doped $Co(OH)_2$ (FeCo) using the same method, with XRD and TEM confirming their successful synthesis (Figure 4d,e; Figures S35–S37, Supporting Information). The catalytic hydrolysis performance for hydrogen production of the three catalysts was evaluated in a 2 wt.% $NaBH_4$ solution. As indicated in Figure 4f, MD-FeCo demonstrates the best SBH performance among these three catalysts. The activation energy

was further investigated by measuring the influence of temperature on the hydrogen generation rate. The results reveal that MD-FeCo exhibits the lowest activation energy for the SBH reaction, calculated to be 31.6 kJ mol^{-1}, while the activation energies for MD-Co and FeCo are 78.4 and 53.5 kJ mol^{-1}, respectively (Figure 4f). Although we did not investigate the optimal ratio of the above-mentioned bimetallic catalysts, the tunable ratio of this method has been demonstrated in the FeNi system. After the loss of molybdate, MD-CoFe and MD-AgCu exhibit higher active surface area and catalytic activity compared to CoFe and AgCu, respectively, as well as superior performance over their monometallic counterparts. All these findings demonstrated the broad applicability of our synthesis strategy for bimetallic catalysts with high active surface area.

3. Conclusion

In summary, we developed a straightforward strategy for synthesizing bimetallic high-activity catalysts with ultra-high electrochemical active surface area through the depletion of Mo. The bimetallic synergistic effect together with high active surface area facilitates the oxidation of Ni^{2+} to higher-valent active species, resulting in the superior OER performance of the obtained MD-FeNi. This strategy has also been validated for broad catalytic applications, for example, CORR and SBH reactions, which provides an effective pathway for the development of high-performance catalysts.

4. Experimental Section

Experimental details are provided in the Supporting Information.

Supporting Information

Supporting Information is available from the Wiley Online Library or from the author.

Acknowledgements

This work was supported by the National Natural Science Foundation of China (22279019). The XAFS was carried out at the 1W1B beamline of the Beijing Synchrotron Radiation Facility (BSRF) and the authors thank Prof. Lirong Zheng for the assistance in the XAS measurements. The authors thank Yifei Xu, Junfeng Chen, and Yajie Zhu for providing suggestions for experiments and articles.

Conflict of Interest

The authors declare no conflict of interest.

Data Availability Statement

The data that support the findings of this study are available from the corresponding author upon reasonable request.

Keywords

anion-exchange membrane water electrolysis, bimetallic catalyst, broad applicability, molybdate-leaching, oxygen evolution reaction

Received: March 3, 2025
Revised: April 8, 2025
Published online:

[1] M. Klingenhof, H. Trzesniowski, S. Koch, J. Zhu, Z. Zeng, L. Metzler, A. Klinger, M. Elshamy, F. Lehmann, P. W. Buchheister, A. Weisser, G. Schmid, S. Vierrath, F. Dionigi, P. Strasser, *Nat. Catal.* **2024**, *7*, 1213.
[2] Z. Li, G. Lin, L. Wang, H. Lee, J. Du, T. Tang, G. Ding, R. Ren, W. Li, X. Cao, S. Ding, W. Ye, W. Yang, L. Sun, *Nat. Catal.* **2024**, *7*, 944.
[3] P. Chen, X. Hu, *Adv. Energy Mater.* **2020**, *10*, 2002285.
[4] Z. W. Seh, J. Kibsgaard, C. F. Dickens, I. Chorkendorff, J. K. Nørskov, T. F. Jaramillo, *Science* **2017**, *355*, aad4998.
[5] C. Liang, P. Zou, A. Nairan, Y. Zhang, J. Liu, K. Liu, S. Hu, F. Kang, H. J. Fan, C. Yang, *Energy Environ. Sci.* **2020**, *13*, 86.
[6] J. Suntivich, K. J. May, H. A. Gasteiger, J. B. Goodenough, Y. Shao-Horn, *Science* **2011**, *334*, 1383.
[7] Z. Zhang, L. Song, *Chin. J. Eng.* **2025**, *47*, 282.
[8] J. Song, C. Wei, Z.-F. Huang, C. Liu, L. Zeng, X. Wang, Z. J. Xu, *Chem. Soc. Rev.* **2020**, *49*, 2196.
[9] Y. Nakaya, S. Furukawa, *Chem. Rev.* **2023**, *123*, 5859.
[10] A. Pedersen, J. Barrio, A. Li, R. Jervis, D. J. L. Brett, M. M. Titirici, I. E. L. Stephens, *Adv. Energy Mater.* **2022**, *12*, 2102715.
[11] P. Buchwalter, J. Rosé, P. Braunstein, *Chem. Rev.* **2015**, *115*, 28.
[12] Y. Bing, H. Liu, L. Zhang, D. Ghosh, J. Zhang, *Chem. Soc. Rev.* **2010**, *39*, 2184.
[13] L. Liu, A. Corma, *Chem. Rev.* **2023**, *123*, 4855.
[14] W. Niu, Z. Chen, W. Guo, W. Mao, Y. Liu, Y. Guo, J. Chen, R. Huang, L. Kang, Y. Ma, Q. Yan, J. Ye, C. Cui, L. Zhang, P. Wang, X. Xu, B. Zhang, *Nat. Commun.* **2023**, *14*, 4882.
[15] Y. Ji, Z. Chen, R. Wei, C. Yang, Y. Wang, J. Xu, H. Zhang, A. Guan, J. Chen, T.-K. Sham, J. Luo, Y. Yang, X. Xu, G. Zheng, *Nat. Catal.* **2022**, *5*, 251.
[16] H. Li, Y. Lin, J. Duan, Q. Wen, Y. Liu, T. Zhai, *Chem. Soc. Rev.* **2024**, *53*, 10709.
[17] J. Feng, X. Wang, H. Pan, *Adv. Mater.* **2024**, *36*, 2411688.
[18] M. E. Coller Pascuzzi, A. Goryachev, J. P. Hofmann, E. J. M. Hensen, *Appl. Catal. B* **2020**, *261*, 118225.
[19] X. Bo, R. K. Hocking, S. Zhou, Y. Li, X. Chen, J. Zhuang, Y. Du, C. Zhao, *Energy Environ. Sci.* **2020**, *13*, 4225.
[20] A. Rajput, M. K. Adak, B. Chakraborty, *Inorg. Chem.* **2022**, *61*, 11189.
[21] Y. Zhu, C. Liu, S. Cui, Z. Lu, J. Ye, Y. Wen, W. Shi, X. Huang, L. Xue, J. Bian, Y. Li, Y. Xu, B. Zhang, *Adv. Mater.* **2023**, *35*, 2301549.
[22] Y. Wang, L. Yan, K. Dastafkan, C. Zhao, X. Zhao, Y. Xue, J. Huo, S. Li, Q. Zhai, *Adv. Mater.* **2021**, *33*, 2006351.
[23] J.-H. Kim, D. H. Youn, K. Kawashima, J. Lin, H. Lim, C. B. Mullins, *Appl. Catal. B* **2018**, *225*, 1.
[24] J. Jiang, X.-L. Zhou, H.-G. Lv, H.-Q. Yu, Y. Yu, *Adv. Funct. Mater.* **2023**, *33*, 2212160.
[25] C. Huang, Q. Zhou, L. Yu, D. Duan, T. Cao, S. Qiu, Z. Wang, J. Guo, Y. Xie, L. Li, Y. Yu, *Adv. Energy Mater.* **2023**, *13*, 2301475.
[26] Y. Dong, P. Zhang, Y. Kou, Z. Yang, Y. Li, X. Sun, *Catal. Lett.* **2015**, *145*, 1541.
[27] B. S. Yeo, A. T. Bell, *J. Am. Chem. Soc.* **2011**, *133*, 5587.
[28] Q. Zhao, J. Yang, M. Liu, R. Wang, G. Zhang, H. Wang, H. Tang, C. Liu, Z. Mei, H. Chen, F. Pan, *ACS Catal.* **2018**, *8*, 5621.
[29] J. Zhang, M. Li, Z. Qiao, K. Huo, Y. Yang, D. Ji, D. Yuan, L. Lin, Z. Li, H. Wu, *J. Mater. Chem. A* **2024**, *12*, 2044.
[30] L. Trotochaud, S. L. Young, J. K. Ranney, S. W. Boettcher, *J. Am. Chem. Soc.* **2014**, *136*, 6744.
[31] W.-J. Jiang, T. Tang, Y. Zhang, J.-S. Hu, *Acc. Chem. Res.* **2020**, *53*, 1111.
[32] R. N. Dürr, P. Maltoni, H. Tian, B. Jousselme, L. Hammarström, T. Edvinsson, *ACS Nano* **2021**, *15*, 13504.

[33] X. Liu, J. Meng, K. Ni, R. Guo, F. Xia, J. Xie, X. Li, B. Wen, P. Wu, M. Li, J. Wu, X. Wu, L. Mai, D. Zhao, *Cell Rep. Phys. Sci.* **2020**, *1*, 100241.
[34] Y. Yao, G. Zhao, X. Guo, P. Xiong, Z. Xu, L. Zhang, C. Chen, C. Xu, T.-S. Wu, Y.-L. Soo, Z. Cui, M. M.-J. Li, Y. Zhu, *J. Am. Chem. Soc.* **2024**, *146*, 15219.
[35] S. Lee, Y.-C. Chu, L. Bai, H. M. Chen, X. Hu, *Chem Catal.* **2023**, *3*, 100475.
[36] D. S. Hall, D. J. Lockwood, S. Poirier, C. Bock, B. R. MacDougall, *J. Phys. Chem. A.* **2012**, *116*, 6771.
[37] C. Liu, Y. Li, *J. Alloys Compd.* **2009**, *478*, 415.
[38] J. Hu, S. Li, J. Chu, S. Niu, J. Wang, Y. Du, Z. Li, X. Han, P. Xu, *ACS Catal.* **2019**, *9*, 10705.
[39] D. L. A. de Faria, S. Venâncio Silva, M. T. de Oliveira, *J. Raman Spectrosc.* **1997**, *28*, 873.
[40] Z. Gong, X. Wang, W. Pi, N. Yao, Z. Fang, H. Bao, Q. Wu, *Mater. Today Phys.* **2024**, *43*, 101399.
[41] B. Ravel, M. Newville, *J. Synchrotron Radiat.* **2005**, *12*, 537.
[42] A. J. Tkalych, K. Yu, E. A. Carter, *J. Phys. Chem. C* **2015**, *119*, 24315.
[43] R. Li, R. Wu, Z. Li, J. Wang, X. Liu, Y. Wen, F.-K. Chiang, S.-W. Chen, K. C. Chan, Z. Lu, *Adv. Mater.* **2023**, *35*, 2206890.
[44] H. Yuan, C. Weng, X. Zhang, L. Chen, Q. Zhang, L. Ma, J. Liu, *Mater. Today Phys.* **2024**, *49*, 101601.
[45] P. B. O'Mara, P. Wilde, T. M. Benedetti, C. Andronescu, S. Cheong, J. J. Gooding, R. D. Tilley, W. Schuhmann, *J. Am. Chem. Soc.* **2019**, *141*, 14093.
[46] X. Wang, P. Ou, A. Ozden, S.-F. Hung, J. Tam, C. M. Gabardo, J. Y. Howe, J. Sisler, K. Bertens, F. P. García de Arquer, R. K. Miao, C. P. O'Brien, Z. Wang, J. Abed, A. S. Rasouli, M. Sun, A. H. Ip, D. Sinton, E. H. Sargent, *Nat. Energy* **2022**, *7*, 170.